A Numerical Study of the Effects of Wave-Induced Fluid Flow in Porous Media: Linear Solver

Yang Zhang[1], Limin Song [2], Max Deffenbaugh [2] and M. Nafi Toksöz [1]

1: Earth Resources Laboratory
Dept. of Earth, Atmospheric and Planetary Sciences
Massachusetts Institute of Technology
Cambridge, MA 02139

2: ExxonMobil Research and Engineering
Annandale, New Jersey 08801

Abstract

In this paper, we present a computational method to simulate wave propagation in porous rocks saturated with Newtonian fluids over a range of frequencies of interest. The method can use a digital representation of a rock sample where distinct material phase and properties at each volume cell are identified and model the dynamic response of the rock to an acoustic excitation mathematically with a coupled equation system: elastic wave equation in solid matrix and viscous wave equation in fluid. The coupled wave equations are solved numerically with a rotated-staggered-grid finite difference scheme. We simulate P-wave propagation through an idealized porous medium of periodically alternating solid and fluid layers where an analytical solution is available and obtain excellent agreements between numerical and analytical solutions. The method models the effect of pore fluid motion on the rock dynamic response more accurately with a linearized Navier-Stokes equation than with the viscoelastic model of the generalized Maxwell body, a low frequency approximation commonly used to overcome the difficulty of modeling frequency-dependent fluid shear modulus in time domain.

1. Introduction

Intrinsic velocities and attenuations of wave propagation in porous rocks are very important rock properties that are commonly used in depth calibration for surface reflection seismograms, lithology classifications, hydrocarbon identifications, and reservoir management in oil/gas exploration and production industries. However, the effects of pore structures and fluid motion on wave propagation in complex rocks such as carbonate are not well understood. There are increasing needs for developing better understanding of the relationship between acoustic and physical properties of carbonate rocks over a range of frequencies of interest, from seismic to sonic logging to ultrasonic lab measurements.

It is known that the wave-induced motion of viscous fluid in a porous rock causes significant frequency-dependence in both acoustic velocities and attenuation. Different physical mechanisms and theoretical models have been developed in the past to describe the effects of viscous fluid motion on the acoustic dispersion and attenuation. Biot (1956a, b) developed a theory of wave propagation in saturated porous rocks based on a macroscopic fluid-flow model. Biot's theory shows that acoustic waves produce relative motion between the fluid and solid frame due to inertial effects, resulting in viscous attenuation of the acoustic waves. At the low frequency limit of Biot's theory, the viscous layer is much larger than the pore sizes so that fluid and solid virtually move together. At the high frequency limit, the viscous layer is very thin so that fluid is essentially decoupled from the solid frame. At both limiting ends of the frequencies, Biot's theory predicts little dispersion and attenuation. The maximum dispersion and attenuation occurs at the so-called Biot's characteristic frequency which is linearly proportional to the fluid viscosity.

For common fluid-saturated rocks, Biot's characteristic frequency is much higher than seismic and sonic-logging frequencies. Therefore, it is the common practice to apply Gassmann's fluid substitution relation, the low-frequency limit of Biot's theory, to predict the effect of different fluids on the effective elastic properties of the rock. Though prediction from Gassmann's relation fits the experimental data relatively well for simpler rocks such as sandstones (Winkler, 1985), its applicability to carbonate rocks is uncertain. Experimental work (Wang, *et al*., 1991, Assefa, *et al*., 2003) has been done in the past to test the validation of Gassmann's relation for carbonates but most of these experiements involved lab measurements at ultrasonic frequencies. Recently Adam *et al*. (2006) reported some interesting results of laboratory experiments in both seismic and ultrasonic frequencies. Their work shows not only the difference of the elastic properties between seismic and ultrasonic frequencies, but also noticeable dispersion within seismic frequencies (3-3000 Hz) for brine-saturated carbonates, a clear failure of Gassmann's relation. At 100 Hz and low differential pressure of 3.5 MPa, they observed that Gassmann's relation generally over-predicts bulk modulus and under-predicts shear modulus. The deviation between measured and predicted becomes smaller at increasing differential pressure. Though their experimental results are statistically insufficient to reach general conclusions about physical causes of the modulus dispersion and failure of Gassmann's relation, it is clear that the existence of heterogeneous and compliant pores/micro-fractures in the samples and interaction of the fluid with solid grains on the pore-scale play an important role.

Though more lab measurements will be needed to provide insight on the uncertainty in the acoustics properties of carbonates, a recent advance in numerical simulation of the rock physics on the pore-scale may help provide answers to some of the unresolved questions. This numerical simulation approach, commonly called computational rock physics, models the rock physics on the scale of the individual pore and grain out of digital rock images acquired from X-Ray CT scans and computes the effective physical properties of rocks numerically based on fundamental relations. It has been used mostly to model the effect of pores, fractures and fluid on the static elastic properties with the finite element method (Roberts and Garboczi, 2000; Arns *et al*., 2003, Grechka and Kachanov, 2006). Recently it has been used to study acoustic wave velocities and attenuation of the rocks using the finite difference method.

Saenger *et al*. (2005) developed the viscolelastic rotated-staggered-grid (VRSG) algorithm that can perform pore-scale simulation of wave propagation in porous materials saturated with viscous fluid. In their algorithm, they use a single-order generalized Maxwell body (GMB) model to approximate a Newtonian fluid. The time-domain stress-strain relation with the single-order GMB model are defined as

$$\sigma_{ij}(t) = c_{ijkl}\varepsilon_{kl}(t) - \xi_{ij}(t) \tag{1}$$

and

$$\dot{\xi}_{ij} + \omega_r \xi_{ij} = \omega_r Y_{ijkl}\varepsilon_{kl} \tag{2}$$

where σ_{ij} and ε_{kl} are the stresses and strains, c_{ijkl} is the tensor of elastic coefficient or un-relaxed modulus, ξ_{ij} is the anelastic function, ω_r is the angular relaxation frequency, and Y_{ijkl} is the tensor of anelastic coefficients, or defect modulus. In the frequency domain, equations (1) and (2) give rise to the complex moduli simply as

$$C_{ijkl}(\omega) = c_{ijkl} - Y_{ijkl}\frac{\omega_r}{\omega_r + i\omega} \tag{3}$$

The elastic and anelastic coefficients, and relaxation frequency of the GMB model have to be determined appropriately in order to use equations (1) and (2) to simulate wave propagation in time-domain. Saenger *et al*. (2005) approximate the equation (3) with a first-order Taylor series expanded at

$\omega = 0$, and relate it to the behavior of Newtonian fluid at zero frequency. As a result, the following relations are derived as the low frequency limits for the independent coefficients of the GMB model:

$$c_{44} = Y_{44} = \eta_\mu \omega_r \tag{4}$$

$$c_{12} = K_f + \eta_\lambda \omega_r \tag{5}$$

$$Y_{12} = \eta_\lambda \omega_r \tag{6}$$

where K_f is the bulk modulus, η_μ and η_λ are the shear and bulk viscosity of the fluid. Other coefficients can be determined as combinations of the above ones based on isotropic assumption. Given the properties of the fluid, the relaxation frequency is the only remaining parameter to be determined. Since the GMB model is a low-frequency approximation of the Newtonian fluid, it is expected that use of a finite frequency of the excitation source in the numerical simulation will introduce modeling errors. The amount of the errors depends on the ratio of ω / ω_r. To see this clearly, let us substitute the relations (4), (5), and (6) into equation (3), which gives two representative complex moduli:

$$C_{44}(\omega) = i\omega\eta_\mu \frac{1}{1 + i\omega / \omega_r} \tag{7}$$

$$C_{12}(\omega) = K_f + i\omega\eta_\lambda \frac{1}{1 + i\omega / \omega_r} \tag{8}$$

Figure 1a and 1b plot the real and imaginary parts of C_{44}, normalized by the Newtonian shear modulus ($\omega\eta_\mu$). It is clear that two sources of the modeling errors are associated with the GMB: addition of a non-zero real shear modulus that peaks at $\omega = \omega_r$ and reduction in the imaginary shear modulus. The first error would cause propagation of shear waves which do not exist in the Newtonian viscous fluid, while the second would reduce viscosities. It should be noted that the first type of error is relatively larger than the second one. With a sufficient high relaxation frequency such that $\omega << \omega_r$, the GMB model is a good approximation of the dynamic behavior of the Newtonian fluids.

This paper presents an alternative approach to Saenger's VRSG algorithm for modeling wave propagation in porous rock saturated with Newtonian fluid. Instead of modeling the fluid with the GMB, we use linearized Navier-Stokes equations to describe the dynamic motion of the fluid induced by wave propagation. With elastic wave equations for the solids, we numerically solve the coupled equation system by using the finite difference scheme with a rotated-staggered-grid (Saenger, *et al*., 2000). To validate the approach, we simulate P-wave propagation through an idealized porous medium of periodically alternating solid and fluid layers where analytical solutions are available (Ciz, *et al*., 2006). The numerical results agree well with those of the analytical solution.

2. General Governing Equations

We consider a porous rock consisting of a matrix of elastic solid and pores filled with a Newtonian viscous fluid. With a disturbance of small amplitude propagating through the rock, the governing equations for the displacement vector, **u**, of the rock at any point **x** and time t due to the propagation of disturbance are given by

Elastic dynamic equation in solid:

$$\rho_s \frac{\partial \mathbf{u}^2}{\partial t^2} = \nabla\left[(\lambda+\mu)\nabla \bullet \mathbf{u}\right] + \mu\nabla^2\mathbf{u} + \mathbf{f} \tag{9}$$

Linearized Navier-Stokes equation in fluid:

$$\rho_f \frac{\partial \mathbf{u}^2}{\partial t^2} = K_f \nabla\left[\nabla \bullet \mathbf{u}\right] + \frac{\partial}{\partial t}\left[\eta_\mu \nabla^2\mathbf{u} + (\eta_\mu + \eta_\lambda)\nabla\left(\nabla \bullet \mathbf{u}\right)\right] + \mathbf{f} \tag{10}$$

where ρ_s, λ and μ are the density, Lamé elastic constants of solid phase, and ρ_f, K_f, η_μ and η_λ are the density, compressional or bulk modulus, and viscosity coefficients of fluid phase, and vector $\mathbf{f}$ is the volumetric force. The effect of the fluid pressure inside the pore is reflected by the value of K_f. In microscopic or pore scale, it is assumed that material properties of either solid or fluid are homogenous and isotropic but in macroscopic scale, they can be heterogeneous and anisotropic when the rock sample is considered as a whole. Therefore, material properties are, in general, the functions of space. In addition, the equations above can be used to describe a rock composed of multiple solids or fluids.

The equations are coupled through the boundary condition at the interface between adjacent solid and fluid phases. The internal boundary conditions at the inter-phase between the solid and fluid are naturally satisfied by the equilibrium (equal stress) and non-slip (equal displacement) conditions because of the non-zero viscosity. The external boundary condition depends on the loading and environment, and can be described by either traction or displacement conditions.

From the point view of numerical simulation, it is advantageous to use a single equation to describe the wave propagation in either solid or fluid phase. To do so, let us consider a finite sample of porous rock with a domain of the rock medium Ω and a boundary Γ. We can use a more general equation as follows

$$\rho \frac{\partial u_i^2}{\partial t^2} = \frac{\partial \sigma_{ij}}{\partial x_j} + f_i \quad \text{in} \quad \Omega \tag{11}$$

with general external boundary conditions on the surface of the rock sample as follows

$$u_i = g_i \quad \text{on} \quad \Gamma_{gi} \tag{12}$$

and

$$\sigma_{ij} = h_i \quad \text{on} \quad \Gamma_{hi} \tag{13}$$

and initial conditions

$$u_i(x, t=0) = u_{0i} \tag{14}$$

and

$$\frac{\partial u_i(x, t=0)}{\partial t} = \dot{u}_{oi} \tag{15}$$

Comparing and combining the equations (9) and (10), we can write the constitution equation or stress tensor as

$$\sigma_{ij} = \delta_{ij} a_p \varepsilon_{kk} + 2 b_p \varepsilon_{ij} + \delta_{ij} \alpha_p \dot{\varepsilon}_{kk} + 2 \beta_p \dot{\varepsilon}_{ij} \tag{16}$$

where the strain and strain rate tensors are defined as

$$\varepsilon_{ij} = \frac{1}{2}\left(\frac{\partial u_i}{\partial x_j} + \frac{\partial u_j}{\partial x_i} \right) \tag{17}$$

and

$$\dot{\varepsilon}_{ij} = \frac{\partial \varepsilon_{ij}}{\partial t} \tag{18}$$

The coefficients of the constitution equation (16) are given, depending on the phase, as

If p = isotropic solid phase, then

$$\begin{aligned} a_p &= \lambda, \quad b_p = \mu \\ \alpha_p &= 0, \quad \beta_p = 0 \end{aligned} \tag{19}$$

If p = Newtonian fluid phase, then

$$\begin{aligned} a_p &= K_f, \quad b_p = 0 \\ \alpha_p &= \eta_\lambda, \quad \beta_p = \eta_\mu \end{aligned} \tag{20}$$

Furthermore, we can rewrite the stress and strain tensors in the vectors as

$$\boldsymbol{\sigma} = \left\{ \sigma_{11}, \sigma_{22}, \sigma_{33}, \sigma_{23}, \sigma_{13}, \sigma_{12} \right\}^T \tag{21}$$

and

$$\boldsymbol{\varepsilon} = \left\{ \varepsilon_{11}, \varepsilon_{22}, \varepsilon_{33}, \varepsilon_{23}, \varepsilon_{13}, \varepsilon_{12} \right\}^T \tag{22}$$

Then we obtain the constitution equation as

$$\boldsymbol{\sigma} = \mathbf{D}\boldsymbol{\varepsilon} + \mathbf{E}\dot{\boldsymbol{\varepsilon}} \tag{23}$$

where the matrices are simply given by

$$\mathbf{D} = \begin{Bmatrix} a_p + 2b_p & a_p & a_p & 0 & 0 & 0 \\ a_p & a_p + 2b_p & a_p & 0 & 0 & 0 \\ a_p & a_p & a_p + 2b_p & 0 & 0 & 0 \\ 0 & 0 & 0 & 2b_p & 0 & 0 \\ 0 & 0 & 0 & 0 & 2b_p & 0 \\ 0 & 0 & 0 & 0 & 0 & 2b_p \end{Bmatrix} \tag{24}$$

and

$$\mathbf{E} = \begin{Bmatrix} \alpha_p + 2\beta_p & \alpha_p & \alpha_p & 0 & 0 & 0 \\ \alpha_p & \alpha_p + 2\beta_p & \alpha_p & 0 & 0 & 0 \\ \alpha_p & \alpha_p & \alpha_p + 2\beta_p & 0 & 0 & 0 \\ 0 & 0 & 0 & 2\beta_p & 0 & 0 \\ 0 & 0 & 0 & 0 & 2\beta_p & 0 \\ 0 & 0 & 0 & 0 & 0 & 2\beta_p \end{Bmatrix} \tag{25}$$

Numerically, the system of equations of (11)-(25) can be solved to simulate the displacement field provided that the material properties and pore geometries and arrangements in the space are known. The high-resolution 3D X-ray micro-tomography images of rock samples provide detailed information for such numerical simulations. Our main interest in numerical simulations of the porous rock dynamics in microscopic scale is to determine the effective acoustic properties (velocity dispersion and attenuation) of the rock in macroscopic scale.

3. Numerical Implementation

To couple the wave equations with the linearized Navier-Stokes equations (WLNS), we choose a velocity-stress scheme to solve the wave equations in solid domain. The advantage of using this scheme is to solve velocities both in solid and fluid domains, which makes the coupling of these two domains much easier. In such a way, equations (9) and (23) can be expressed as:

$$\rho_s \frac{\partial \mathbf{v}}{\partial t} = \nabla \cdot \boldsymbol{\sigma} + \mathbf{f} \tag{26}$$

$$\dot{\sigma} = \mathbf{D}\dot{\boldsymbol{\varepsilon}} \tag{27}$$

where $\mathbf{v}$ is the velocity in the solid domain, $\dot{\sigma}$ and $\dot{\varepsilon}$ are the rates of stress and strain. While in the fluid domain, as described in the previous section, we have:

$$\rho_f \frac{\partial \mathbf{v}}{\partial t} = \nabla \cdot \boldsymbol{\sigma} + \mathbf{f} \tag{28}$$

$$\boldsymbol{\sigma} = \mathbf{E}\dot{\boldsymbol{\varepsilon}} \tag{29}$$

In this paper, we numerically couple these two systems by using the finite difference method. For finite difference solvers in the time domain, the standard-staggered-grid (SSG) scheme is the one usually used, which averages the shear moduli of the nearby cells to update the shear stress, as shown in Figure 2. This gives rise to the difficulty of calculating the interface between the solid and fluid domains because of the coexistence of the real number of the shear modulus μ in the solid side and the complex number of frequency-dependent $\mu_f = i\omega\eta$ in the fluid side. Averaging of the shear moduli across the interface can introduce frequency-dependent moduli into the calculation. Calculating stresses with frequency-dependent moduli in the frequency domain is equal to calculating convolutions between moduli and strains in the time domain – which is time and memory consuming in numerical modeling. One way to tackle the frequency-dependent moduli in the time domain is to use the general Maxwell body (GMB) model to represent anelastic effects (Emmerich and Korn, 1987).

Instead of using the SSG scheme, we chose the rotated-staggered-grid (RSG) scheme (Saenger, *et al*., 2000) to handle the interface problem occurring in the SSG scheme. As shown in Figure 3, in the RSG

scheme, all the stresses are at the center of each cell and velocities are at the corners. For cells located in the solid, we put elastic moduli at the center, and for those in the fluid, we put viscosities and bulk modulus of fluid at center. The advantage of using the RSG scheme is that it does not need to average shear moduli, which means that, in our coupled model, there is no need to use the complex number of $\mu_f = i\omega\eta$ in cells in the fluid domain that are close to boundaries. In this way, we can solve the wave equations and the linearized Navier-Stokes equations (WLNS) separately without introducing frequency-dependent moduli. The coupling between these two systems is fulfilled naturally by the continuities of velocities and stresses on the boundaries, as shown in Figure 4.

The finite difference method of solving the wave equations by using the RSG scheme has been established by Saenger *et al*. (2000). In order to solve the linearized Navier-Stokes equations, we begin with updating stress tensor $\boldsymbol{\sigma}$, which is related to pressure p and velocity $\mathbf{v}$ by bulk modulus K_f and viscosities η_μ and η_λ. From equation (10) and (29), we can see that the way to update stress tensor $\boldsymbol{\sigma}$ can be:

$$\sigma_{ij} = -p\delta_{ij} + \left[\eta_\mu \left(\frac{\partial v_i}{\partial x_j} + \frac{\partial v_j}{\partial x_i} \right) + \eta_\lambda \frac{\partial v_k}{\partial x_k} \delta_{ij} \right] \tag{30}$$

$$\frac{\partial p}{\partial t} = -K_f \frac{\partial v_k}{\partial x_k} \tag{31}$$

where an intermediate step for updating pressure is needed. Assuming we know pressure $p(t-\frac{1}{2})$ at time $(t-\frac{1}{2})$ and velocities $v_i(t)$ at time t, we can update the pressure field $p(t+\frac{1}{2})$ at time $(t+\frac{1}{2})$ by using equation (31), and then with the new pressure $p(t+\frac{1}{2})$ and the known velocities, we can calculate the stresses by equation (30); finally we can update the velocities $v(t+1)$ at time $(t+1)$ by using equation (28).

4. Numerical Validation of The Coupled Model

In order to validate our coupled model, we choose a model with periodically alternating solid and viscous fluid layers as a benchmark. This layered model can be considered as an idealized porous medium and has analytic solutions for velocity and attenuation for the compressional wave (Ciz, *et al*., 2006, see also Appendix A).

As shown in Figure 5, one two-layered model with one solid layer and one viscous fluid layer is introduced in our numerical validation. Periodic boundary conditions are applied on both top and bottom, which represent periodic layers of solid and fluid extending into infinity. The modeling parameters are listed in Table I. We use a compressional plane wave as the source, and for calculating the velocities and attenuations, three lines of receivers are deployed in such a way that lines R1 and R2 are separated by 1000 grid points, and R1 and R3 are separated by one wavelength. We chose peaks of waveforms to measure the travel time delay between R1 and R2 for estimating effective velocities, and the amplitude change between R1 and R3 for estimating attenuation of $1/Q$ by assuming a constant Q model. A snapshot of wave propagating in such an idealized porous medium at some time step is shown in Figure 6, from which we can see that the compressional wave traveling in solid induces particle motion in fluid along the interface within certain skin depth. This type of friction between solid and fluid interface actually plays an important role in causing wave dispersion and attenuation. Also due to the fast wave speed of solid, the compressional wave in fluid moves faster close to the interface than in the middle part of the wave front.

We then compare the results from the coupled model with those of analytic solutions, as shown in Figure 7 for effective velocities and Figure 8 for attenuation. From Figure 7, we can see that at higher viscosities, the velocities and attenuations estimated from the coupled model agree well with those of analytic ones. While the estimations from the coupled model deviate from the analytic ones at lower viscosities. The lower the viscosity is, the larger the discrepancy is, which can be attributed to insufficient sampling of the viscous boundary layer that becomes much thinner at low viscosity. According to Ciz *et al*. (2006), at least 3 grids inside the boundary layer are needed to minimize this kind of numerical dispersion. However, in the case with $\eta_\mu = 0.01$ kg/ms, for example, there is less than one grid sampling the boundary layer for m, which is not sufficient according to this criterion. When we increase the sampling within skin depth by using m, we can obtain good estimations of velocities and attenuation again. At the relatively higher viscosities, the attenuations estimated agree with the analytic solutions well because of sufficient sampling in the boundary layer.

Since the GMB model (Saenger, *et al*., 2005) is a low-frequency approximation method, we can expect the discrepancy between the results of our fully coupled model and the GMB model for cases with relative higher source frequency and greater viscosity of fluid. As an example, for a case with source frequency of 500 kHz and $\eta_\mu = 100$ kg/ms, four groups of traces received at different distances from the source are shown in Figure 9. We can see that the differences between traces from the coupled model and the GMB model increase with increasing distance. These differences cannot be ignored especially when we try to measure the attenuation of seismic waves due to the viscosity of fluid.

These comparisons validate that our coupled model can accurately model the effect of viscous fluid, especially at higher frequency and greater viscosity. However, by directly coupling the wave equations and the linearized Navier-Stokes equations, the coupled model gives us more physical insights into the relative interaction between the solid and the fluid when a seismic wave passes by.

5. **Stability of The Coupled Model**

In the coupled model, with using finite difference operators, it is necessary to satisfy certain criteria between grid spacing Δx and time increment Δt so as to make the numerical calculation stable. The relation between Δx and Δt in solving the wave equations is well known (Saegner, *et al*., 2000), and we derive the stability criteria for the linearized Navier-Stokes equations in this paper (see Appendix B for the details for a 2D case). Numerically solving the quartic equation (B.8) by using the Eigenvalue method (Press, *et al*., 1992) can give us four roots $g = \{\lambda_1, \lambda_2, \lambda_3, \lambda_4\}$, which are real or complex values. The stability criterion requires the absolute values of these four roots to be less than one, as described in equation (B.14).

Figure 10 and Figure 11 show the distribution of four roots in the complex coordinate plane with respect to combinations of wavenumber (k_x, k_z). We can see that given the same physical properties of viscous fluid and grid spacing Δx, all four roots can be within the unit circle for cases with smaller Δt (Figure 11) and the computation can be stable, while for cases with larger Δt, some roots, like λ_1 and λ_3 in Figure 10, are outside of the unit circle and the computation becomes unstable.

As we know that the stable region for solving wave equations depends not only on Δt and Δx but also on the velocities of materials, analogously the stable region for solving the linearized Navier-Stokes equations also depends on the viscosities of fluid. As shown in Figures 11 - 13, keeping Δx and Δt the same while increasing the viscosities of fluid, the distribution of the roots changes from where all roots are within the unit circle to where some roots step outside of it, which means that the computation becomes unstable with increase of viscosities.

Compared to the analysis applied to the wave equation, the von Neumann analysis of the linearized Navier-Stokes equations becomes more complicated such that it is not easy to obtain a simple analytic relation among Δt, Δx and the physical properties of viscous fluid to provide guidance for how to choose these values to make the computation stable. However, we can numerically calculate the stable and unstable regions for cases with different combinations of Δt, Δx and the physical properties of viscous fluid, as shown in Figure 14. In the stable region, the absolute values of all roots are ensured to be less than one, and in the unstable region, the absolute values of at least one root are larger than one.

As shown in Figure 14 in a log-log scale, we can see that for larger grid spacing Δx, the relation between Δt and Δx is linear in log-log scale for any value of viscosity, while it becomes nonlinear for smaller grid spacing and larger viscosity. It is worth noting that for relative smaller viscosities ($\eta_\mu \le 0.1$ kg/ms), which cover most of the fluids in nature that we are interested in, the relation stays linear even for smaller grid spacing. As a result, once the computation is stable for a particular combination of (Δt, Δx, η_μ) where $\eta_\mu \le 0.1$, it will be stable for other combinations of ($\Delta t'$, $\Delta x'$, η_μ') which can be derived based on the linear relationship among them. Since in most studies of computational rock physics the grid space of the digital rocks is in order of 10^{-6} m, the linear relation between Δt and Δx for smaller viscosities is helpful.

6. **Conclusions**

In this paper, we developed a multi-phase model by explicitly coupling the wave equations and the linearized Navier-Stokes equations to study the effects of wave-induced particle motion of viscous fluid on seismic velocities and attenuations in porous rocks. The whole coupled system is solved by using the finite difference method with implementation of the rotated-staggered-grid scheme. Compared to the GMB model with a low-frequency approximation, our coupled model gives more accurate results by fully taking into account the viscosity of fluid. A benchmark carried out on an idealized porous medium, a model with periodically alternating solid and viscous fluid layers, shows excellent agreement of results calculated by the coupled model with the analytic solutions both for velocities and attenuations of compressional waves. Also compared to the results from the GMB model, we can see that the attenuation estimation from the GMB model can be different from our coupled model for cases with higher frequency and greater viscosity of fluids. We investigated the numerical stability by doing von Neumann analysis for the linearized Navier-Stokes equations, and found out that there is a linear relation in log-log scale between grid spacing Δx and time increment Δt for cases when the viscosity of the fluid is small ($\eta_\mu \le 0.1$ kg/ms).

Acknowledgements

This work was supported by Schlumberger Doll Research and the MIT Earth Resources Laboratory Founding Member Consortium.

APPENDEIX A: ANALYTIC SOLUTION FOR DISPERSION AND ATTENTION OF COMPRESSIONAL WAVE IN IDEALIZED POROUS MEDIUM

Propagation of the compressional wave in an idealized porous medium with periodically alternating solid and viscous fluid layers denoted by s and f is governed by (Brekhovskikh, 1981; Ciz, *et al*., 2006):

$$\begin{aligned} 4\left(\mu_s-\mu_f\right)^2 K_1K_2+\omega^2\rho_s\left[c^2\rho_s-4\left(\mu_s-\mu_f\right)\right]K_2\tan\frac{\beta_s h_s}{2}+\omega^2\rho_f\left[c^2\rho_f\right. \\ \left.+4\left(\mu_s-\mu_f\right)\right]K_1\tan\frac{\beta_f h_f}{2} \\ -\omega^2\rho_f\rho_s c^2\left[L_1\tan\frac{\beta_f h_f}{2}+L_2\tan\frac{\beta_s h_s}{2}\right]=0 \end{aligned} \tag{A.1}$$

$$\begin{aligned} K_1&=\frac{\omega^2}{c^2}\tan\frac{\beta_s h_s}{2}+\alpha_s\beta_s\tan\frac{\alpha_s h_s}{2} \\ K_2&=\frac{\omega^2}{c^2}\tan\frac{\beta_f h_f}{2}+\alpha_f\beta_f\tan\frac{\alpha_f h_f}{2} \\ L_1&=\frac{\omega^2}{c^2}\tan\frac{\beta_s h_s}{2}-\alpha_f\beta_s\tan\frac{\alpha_f h_f}{2} \\ L_2&=\frac{\omega^2}{c^2}\tan\frac{\beta_f h_f}{2}-\alpha_s\beta_f\tan\frac{\alpha_s h_s}{2} \end{aligned} \tag{A.2}$$

where $\alpha_s^2=\omega^2(1/c_s^2-1/c^2)$, $\alpha_f^2=\omega^2\left(1/c_f^2-1/c^2\right)$ and $c_s=[(K_s+4\mu_s/3)/\rho_s]^{1/2}$, $c_f=\left[\left(K_f+4\mu_f/3\right)/\rho_f\right]^{1/2}$ are compressional velocity in solid and fluid, respectively, and $\beta_s^2=\omega^2(1/b_s^2-1/c^2)$, $\beta_f^2=\omega^2\left(1/b_f^2-1/c^2\right)$ and $b_s=[\mu_s/\rho_s]^{1/2}$, $b_f=\left[\mu_f/\rho_f\right]^{1/2}$ are shear velocity in the solid and fluid, respectively. $\mu_f=-i\omega\eta$ and $K_f=\lambda_f+2\mu_f/3$. h_s and h_f are the thickness of solid and fluid layers, respectively. c is the speed of compressional wave propagating in such system. Once we obtain c, we can estimate the wave attenuation by

$$\frac{1}{Q_P}=\frac{\mathrm{Im}c^{-2}}{\mathrm{Re}c^{-2}} \tag{A.3}$$

APPENDEIX B: STABILITY ANALYSIS FOR LINEARIZED NAVIER-STOKES EQUATIONS IN 2D

In a 2D case, the linearized Navier-Stokes equations are:

$$\begin{aligned}
\rho_f \frac{\partial v_x}{\partial t} &= -\frac{\partial p}{\partial x} + \frac{\partial \sigma_{xx}}{\partial x} + \frac{\partial \sigma_{xz}}{\partial z} \\
\rho_f \frac{\partial v_z}{\partial t} &= -\frac{\partial p}{\partial z} + \frac{\partial \sigma_{xz}}{\partial x} + \frac{\partial \sigma_{zz}}{\partial z} \\
\frac{\partial p}{\partial t} &= -K_f \left(\frac{\partial v_x}{\partial x} + \frac{\partial v_z}{\partial z} \right) \\
\sigma_{xx} &= \left(2\eta_\mu + \eta_\lambda\right) \frac{\partial v_x}{\partial x} + \eta_\lambda \frac{\partial v_z}{\partial z} \\
\sigma_{zz} &= \eta_\lambda \frac{\partial v_x}{\partial x} + \left(2\eta_\mu + \eta_\lambda\right) \frac{\partial v_z}{\partial z} \\
\sigma_{xz} &= \eta_\mu \left(\frac{\partial v_x}{\partial z} + \frac{\partial v_z}{\partial x} \right)
\end{aligned} \tag{B.1}$$

where v_i, σ_{ij}, p are the velocity, stress rates and pressure field, K_f, ρ_f, η_μ and η_λ are the bulk modulus, density, and the viscosities of viscous fluid. In the implementation of the finite difference scheme with grid spacing Δx and time increment Δt, we can represent these equations above by using discrete difference operators D_t and D_x (Saenger, *et al*., 2000) with 2nd order both in space and time as

$$\begin{aligned}
\rho_f D_t v_x &= -D_x p + D_x \sigma_{xx} + D_z \sigma_{xz} \\
\rho_f D_t v_z &= -D_z p + D_x \sigma_{xz} + D_z \sigma_{zz} \\
D_t p &= -K_f \left(D_x v_x + D_z v_z \right) \\
\sigma_{xx} &= \left(2\eta_\mu + \eta_\lambda\right) D_x v_x + \eta_\lambda D_z v_z \\
\sigma_{zz} &= \eta_\lambda D_x v_x + \left(2\eta_\mu + \eta_\lambda\right) D_z v_z \\
\sigma_{xz} &= \eta_\mu \left(D_z v_x + D_x v_z \right)
\end{aligned} \tag{B.2}$$

In terms of displacement, we can introduce displacements u_x and u_z through relations

$$\begin{aligned}
v_x &= D_t u_x \\
v_z &= D_t u_z
\end{aligned} \tag{B.3}$$

Therefore, we can rewrite and combine the equations (B.2) in displacements as

$$\mathbf{A}u = 0 \tag{B.4}$$

where $\mathbf{A}$, a 2×2 matrix operating on displacement vector $u = \left[u_x, u_z\right]^T$, is given by definition as

$$A=\begin{bmatrix} \rho_f D_{tt}-K_f D_{xx} & -K_f D_{xz}-\left(\eta_\mu+\eta_\lambda{}'\right)D_{txz} \\ -\left(2\eta_\mu+\eta_\lambda\right)D_{txx}-\eta_\mu D_{tzz} & \\ -K_f D_{xz}-\left(\eta_\mu+\eta_\lambda{}'\right)D_{txz} & \rho_f D_{tt}-K_f D_{zz} \\ & -\left(2\eta_\mu+\eta_\lambda\right)D_{tzz}-\eta_\mu D_{txx} \end{bmatrix} \tag{B.5}$$

In the von Neumann stability analysis, we usually assume a time-harmonic plane wave with wavefield

$$\begin{bmatrix} u_x(m,n,l) \\ u_z(m,n,l) \end{bmatrix}=\begin{bmatrix} u_{0x} \\ u_{0z} \end{bmatrix} g(k)^l\, e^{i(k_x m\Delta x+k_z n\Delta z)} \tag{B.6}$$

where we only consider the case of that $\Delta z=\Delta x$. To make the numerical computation stable, we need ensure that

$$\left|g(k)\right|\le 1 \quad \forall k \tag{B.7}$$

The solution for $g(k)$ is obtained by solving equation (B.4), which requires the determinant of the system of equations to be equal zero, i.e. $\det(A)=0$. The determinant then yields a quartic equation of $g(k)$ as

$$g^4+c_3 g^3+c_2 g^2+c_1 g+c_0=0 \tag{B.8}$$

where the coefficients c_i are functions of the physical properties of the viscous fluid, grid spacing and time increment defined as

$$\begin{aligned} c_3 &= \beta_{31}\phi-4 \\ c_2 &= \beta_{22}\phi^2-\beta_{21}\phi+6 \\ c_1 &= -\beta_{12}\phi^2+\beta_{11}\phi-4 \\ c_0 &= \beta_{02}\phi^2-\beta_{01}\phi+1 \end{aligned} \tag{B.9}$$

$$\phi=1-\cos(k_x\Delta x)\cos(k_z\Delta x) \tag{B.10}$$

$$\begin{aligned} \beta_{31} &= \frac{2\pi_1\Delta t^2}{\Delta x^2}+\frac{6\pi_2\Delta t}{\Delta x^2}+\frac{2\pi_3\Delta t}{\Delta x^2} \\ \beta_{22} &= \frac{4\pi_1\pi_2\Delta t^3}{\Delta x^4}+\frac{8{\pi_2}^2\Delta t^2}{\Delta x^4}+\frac{4\pi_2\pi_3\Delta t^2}{\Delta x^4} \\ \beta_{21} &= \frac{4\pi_1\Delta t^2}{\Delta x^2}+\frac{18\pi_2\Delta t}{\Delta x^2}+\frac{6\pi_3\Delta t}{\Delta x^2} \\ \beta_{12} &= \frac{4\pi_1\pi_2\Delta t^3}{\Delta x^4}+\frac{16{\pi_2}^2\Delta t^2}{\Delta x^4}+\frac{8\pi_2\pi_3\Delta t^2}{\Delta x^4} \end{aligned} \tag{B.11}$$

$$\beta_{11} = \frac{2\pi_1 \Delta t^2}{\Delta x^2} + \frac{18\pi_2 \Delta t}{\Delta x^2} + \frac{6\pi_3 \Delta t}{\Delta x^2}$$
$$\beta_{02} = \frac{8{\pi_2}^2 \Delta t^2}{\Delta x^4} + \frac{4\pi_2 \pi_3 \Delta t^2}{\Delta x^4}$$
$$\beta_{01} = \frac{6\pi_2 \Delta t}{\Delta x^2} + \frac{2\pi_3 \Delta t}{\Delta x^2}$$

$$\pi_1 = \frac{K_f}{\rho_f}$$
$$\pi_2 = \frac{\eta_\mu}{\rho_f} \qquad \text{(B.12)}$$
$$\pi_3 = \frac{\eta_\lambda}{\rho_f}$$

Equation (B.8) is associated with four roots of $g = \{\lambda_1, \lambda_2, \lambda_3, \lambda_4\}$ which may be real or complex values. Eigenvalue method (Press, *et al*. 1992) is used to solve this quartic equation, where a Hessenberg matrix is constructed with the coefficients c_i as

$$\mathbf{H} = \begin{bmatrix} -c_3 & -c_2 & -c_1 & -c_0 \\ 1 & 0 & 0 & 0 \\ 0 & 1 & 0 & 0 \\ 0 & 0 & 1 & 0 \end{bmatrix} \qquad \text{(B.13)}$$

The four roots of Equation (B.8) correspond to the four eigenvalues of matrix $\mathbf{H}$. The stability criterion requires these four roots to be satisfied by

$$\begin{Bmatrix} |\lambda_1| \\ |\lambda_2| \\ |\lambda_3| \\ |\lambda_4| \end{Bmatrix} \le 1 \quad \forall (k_x, k_z) \qquad \text{(B.14)}$$

References

Adam, L., Batzle, M. and Brevik, L. 2006. *Gassmann's fluid substitution and shear modulus variability in carbonates at laboratory seismic and ultrasonic frequencies*, Geophysics. 71, 6, F173-F183.

Arns, C.H., Knackstedt, M.A., Pinczewsi, W.V. and Garboczi, E.J. 2002. *Computation of linear elastic properties from microtomographic images: Methodology and agreement between theory and experiment*, Geophysics. 67, 5, 1396-1405.

Assefa, S., McCann, C. and Sothcott, J. 2003. *Velocities of compressional and shear waves in limestones*, Geophys. Prospect. 51, 1, 1-13.

Biot, M.A. 1956a. *Theory of propagation of elastic waves in a fluid saturated porous solid, I. Low frequency range*, J. Acoust. Soc. Am. 28, 168-178.

Biot, M.A. 1956b. *Theory of propagation of elastic waves in a fluid saturated porous solid, II. High frequency range*, J. Acoust. Soc. Am. 28, 179-191.

Brekhovskikh, L.M. 1981. *Waves in Layered Media*, Academic, New York.

Ciz, R., Saenger, E.H., and Gurevich, B. 2006. *Pore scale numerical modeling of elastic wave dispersion and attenuation in periodic systems of alternating solid and viscous fluid layers*, J. Acoust. Soc. Am. 120, 2, 642-648.

Emmerich, H., and Korn, M. (1987). *Incorporation of attenuation into time-domain computations of seismic wave fields,* Geophysics. 52, 1252-1264.

Grechka, V. and Kachanov, M. 2006. *Effective elasticity of rocks with closely spaced and intersecting cracks*, Geophysics. 71, 3, D85-D91.

Press, W.H., Teukolsky, S.A., Vetterling, W.T. and Flannery, B.P. 1992. *Numerical Recipes in C* (Cambridge University Press, London).

Roberts, A.P. and Garboczi, E.J. 2000. *Elastic properties of model porous ceramics*, J. Am. Ceram. Soc. 83, 12, 3041-3048.

Saenger, E. H., Gold, N. and Shapiro, S.A. 2000. *Modeling the propagation of elastic waves using a modified finite-difference grid*, Wave Motion. 31, 1, 77–92.

Saenger, E.H. and Shapiro, S.A. 2005. *Seismic effects of viscous Biot-coupling: Finite difference simulations on micro-scale*, Geophys. Res. Lett. 32, L14310, doi:10.1029/2005GL023222

Wang, Z.J., Hirsche, W.K. and Sedgwick, G. 1991. *Seismic velocities in carbonate rocks*, J. Can. Pet. Technol. 30, 2, 112-122.

Winkler, K.W. 1985. *Dispersion analysis of velocity and attenuation in Berea sandstone*, J. Geophys. Res.. 90, B8, 6793-6800.

Table I: Parameters for numerical modeling with the coupled model (In all the cases, we only consider the situation where $\eta_\lambda = \eta_\mu$).

Material Properties:				
	Vp (m/s)	Vs (m/s)	Density (kg/m^3)	Viscosity η_μ (kg/ms)
Solid	5100	2944	2540	
Fluid	1483	0.0	1000	0.001,0.01,0.1,1,10,100
Parameters for finite difference:				
Periodic boundary conditions applied at the top and bottom of the model; Ricker wavelet: $f_{dom} = 500$ kHz; $\Delta x = 1\times10^{-5}$ m , $\Delta t = 5\times10^{-10}$ s $\Delta x = 2\times10^{-6}$ m , $\Delta t = 1\times10^{-10}$ s				

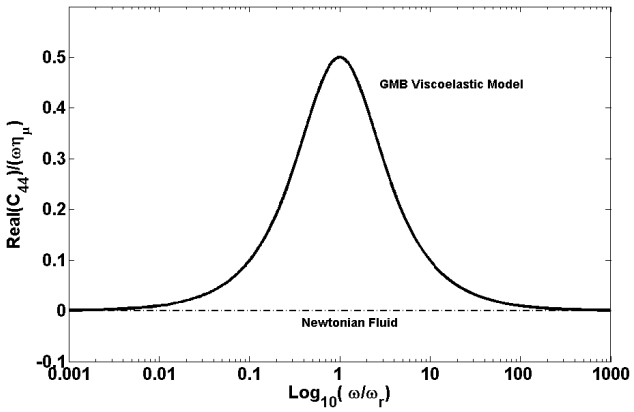

Figure 1a: Real part of C_{44} of GMB model against that of Newtonian fluid, normalized by ($\omega\eta_\mu$)

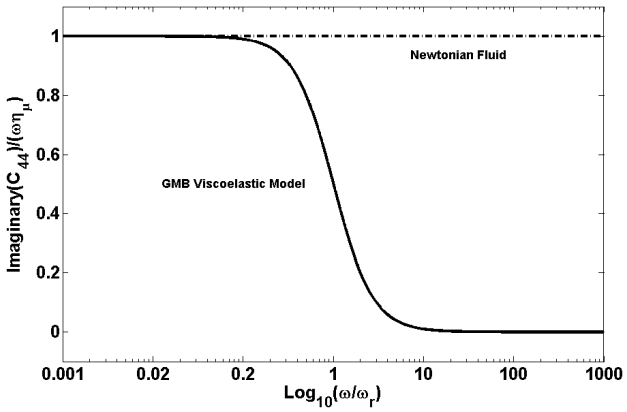

Figure 1b: Imaginary part of C_{44} of GMB model against that of Newtonian fluid, normalized by ($\omega\eta_\mu$)

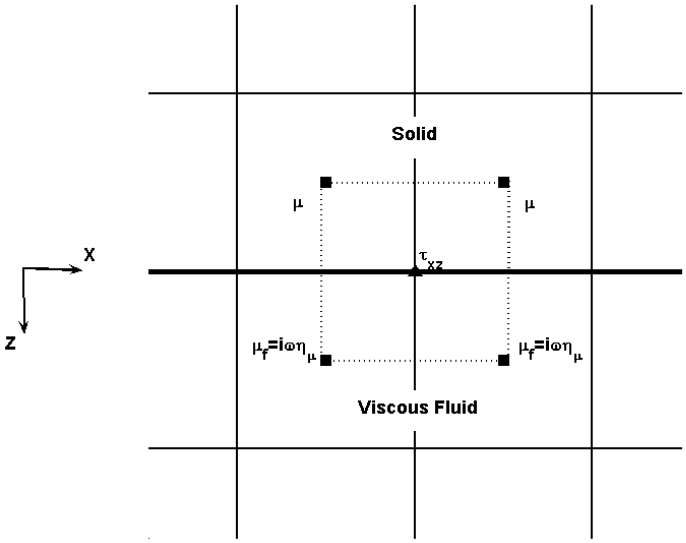

Figure 2: Cells close to the boundary between solid and fluid. Averaging of the shear moduli across the boundary is needed in the standard-staggered-grid, which introduces the complex number of frequency-dependent shear moduli.

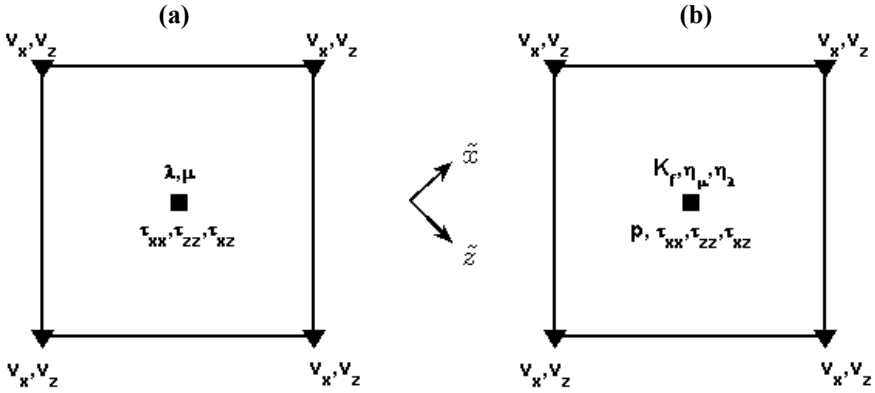

Figure 3: Rotated-staggered-grid scheme for (a) cells in solid and (b) cells in viscous fluid.

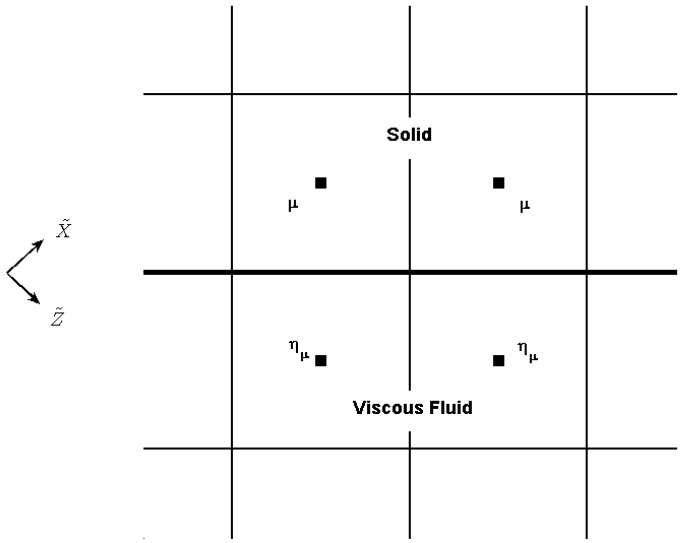

Figure 4: Cells close to the boundary between solid and fluid. Putting the shear modulus and viscosity at the center of each cell, solid and fluid cells can represent themselves respectively. No averaging of shear moduli is involved in the rotated-staggered-grid scheme.

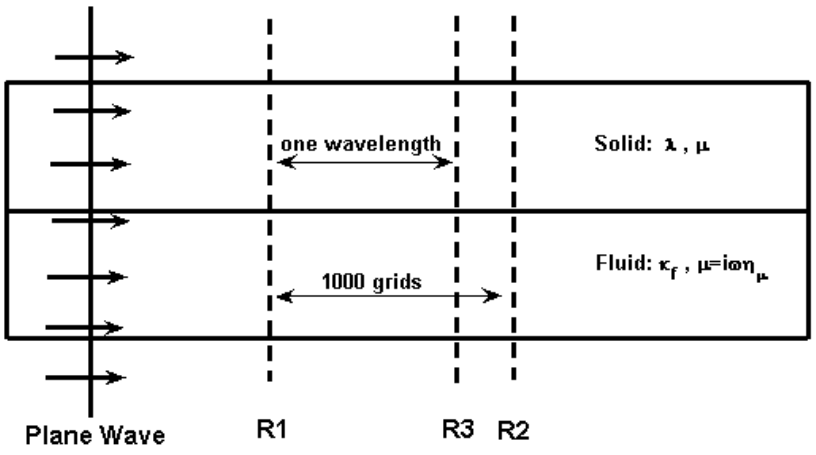

Figure 5: Model with periodically alternating solid and fluid layers. A compressional plane wave is used as the source. Three receiver lines R1, R2 and R3 are deployed. Periodic boundary conditions are applied at the top and bottom of the model.

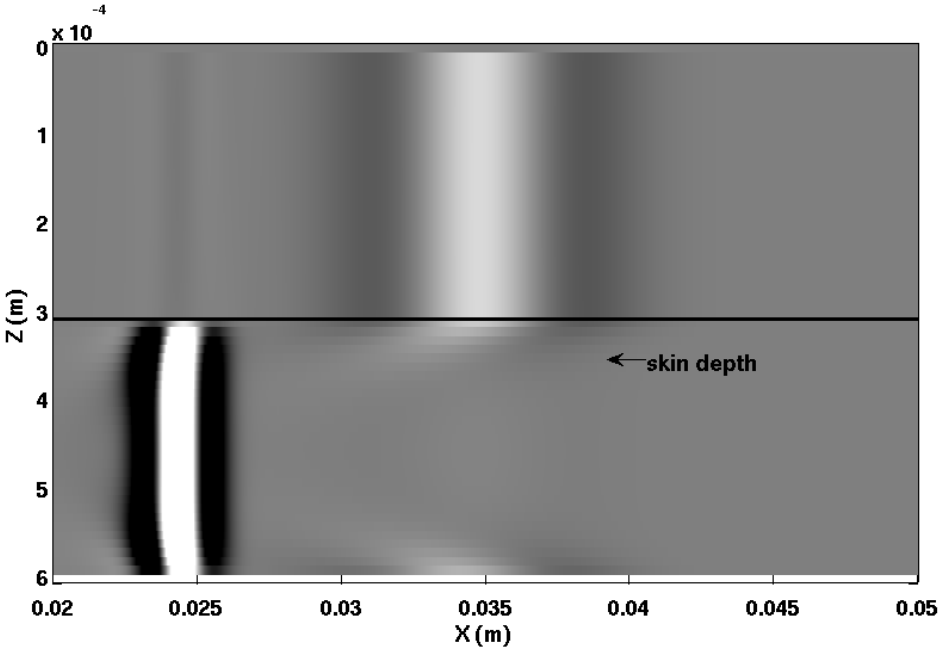

Figure 6: A snapshot of compressional wave propagating in an idealized porous medium at some time step. Waves travel faster in solid (upper half) than those in fluid (lower half). Motion of fluid particles within certain skin depth along interface is induced by wave traveling in solid.

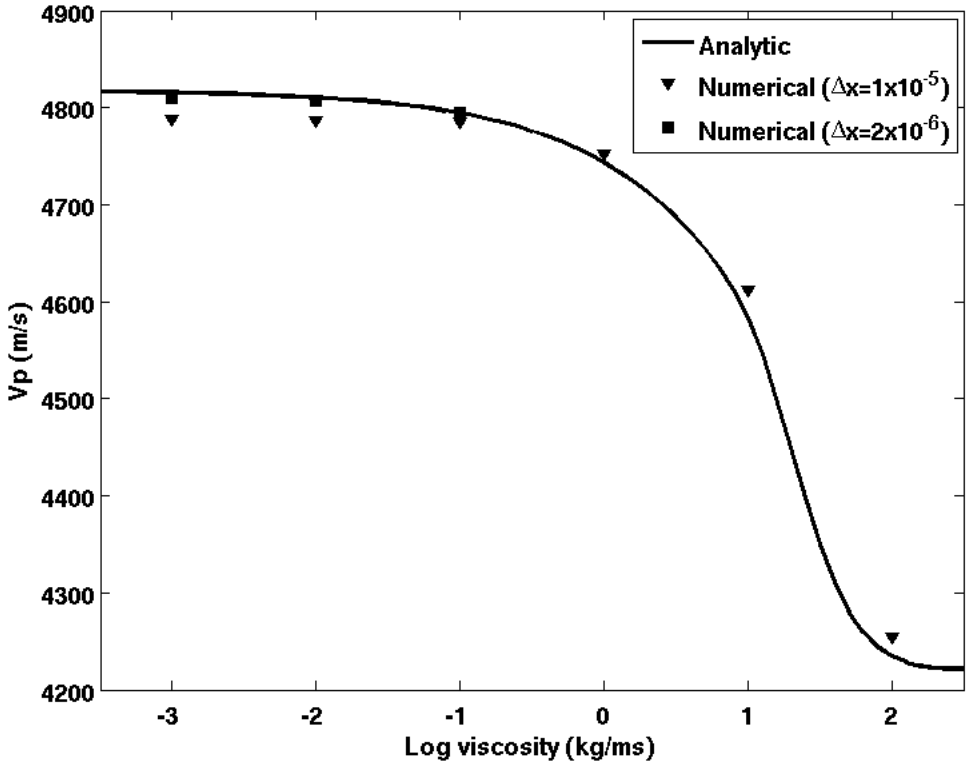

Figure 7: Variations of the velocity of compressional wave with viscosity of fluid. Numerical results calculated with the coupled model (triangle at $\Delta x = 1 \times 10^{-5}$ m and square for $\Delta x = 2 \times 10^{-6}$ m) are compared to analytic solutions (solid curve), which shows a good agreement at higher viscosities. At lower viscosities, because of insufficient sampling of the thin viscous layer at the boundary between the solid and the fluid, numerical dispersion occurs, which can be remedied by increasing sampling within skin depth (square for $\Delta x = 2 \times 10^{-6}$ m.)

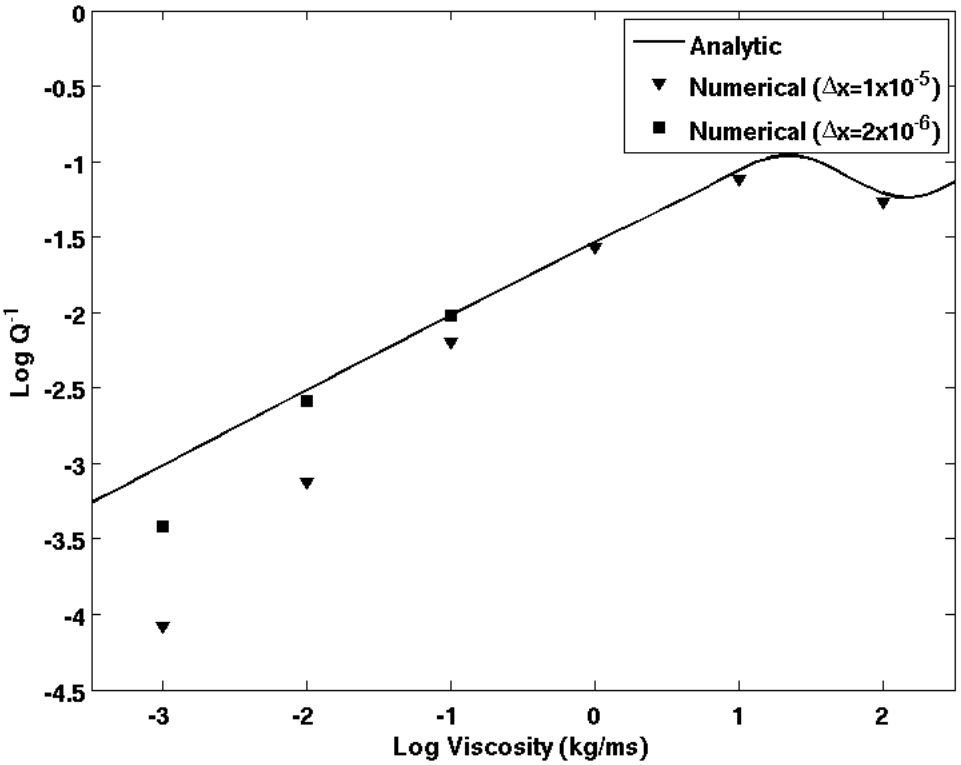

Figure 8: Variations of the attenuation of compressional wave with viscosity of fluid. Numerical results calculated with the coupled model (triangle for $\Delta x = 1 \times 10^{-5}$ m) are compared to analytic solutions (solid curve), which shows a good agreement at higher viscosities. At lower viscosities, because of insufficient sampling of the thin viscous layer at the boundary between the solid and the fluid, numerical dispersion occurs, which can be remedied by increasing sampling within skin depth (square for $\Delta x = 2 \times 10^{-6}$ m.)

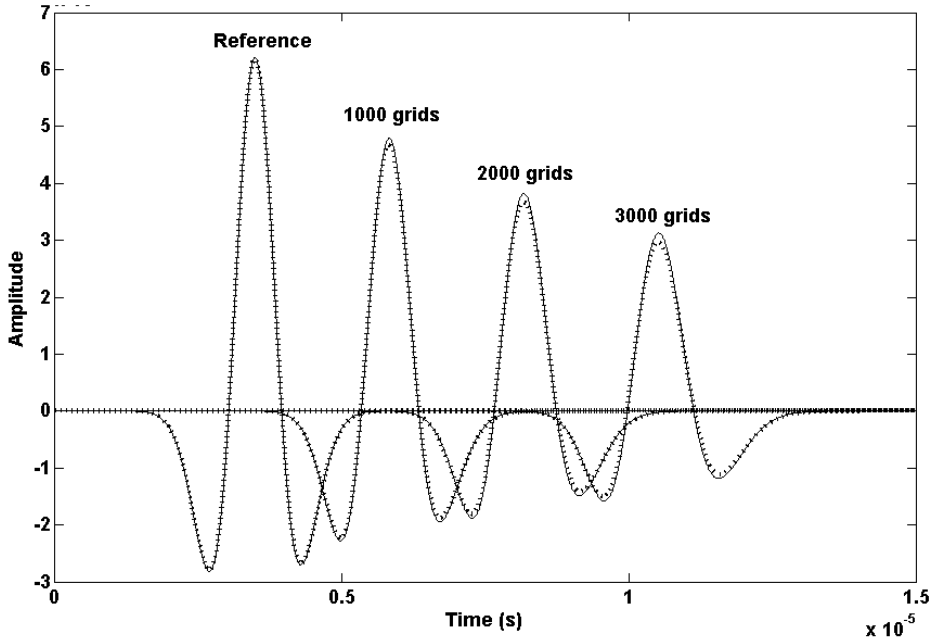

Figure 9: Four groups of traces located at four different distances away from source position are shown. In this case, source frequency of 500 kHz and fluid viscosity $\eta_\mu = 100$ kg/ms are considered. The discrepancies between results from the coupled model (solid curves) and the GMB model (dot curves) increase with distance, which shows that the low-frequency approximation of the GMB model might not accurately estimate the attenuation factor of $1/Q$ for cases with relatively higher source frequency and greater viscosity.

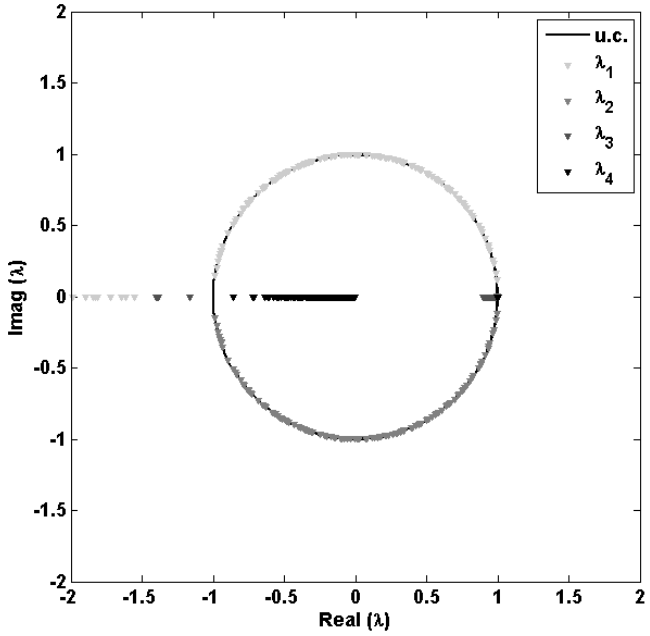

Figure 10: Distribution of the four roots in the complex coordinate plane with respect to combinations of wavenumber (k_x, k_z). The model considered is viscous fluid with $\Delta x = 2\times10^{-6}$ m, $\eta_\mu = 0.01$ kg/ms, and a relative larger $\Delta t = 1\times10^{-8}$ s.

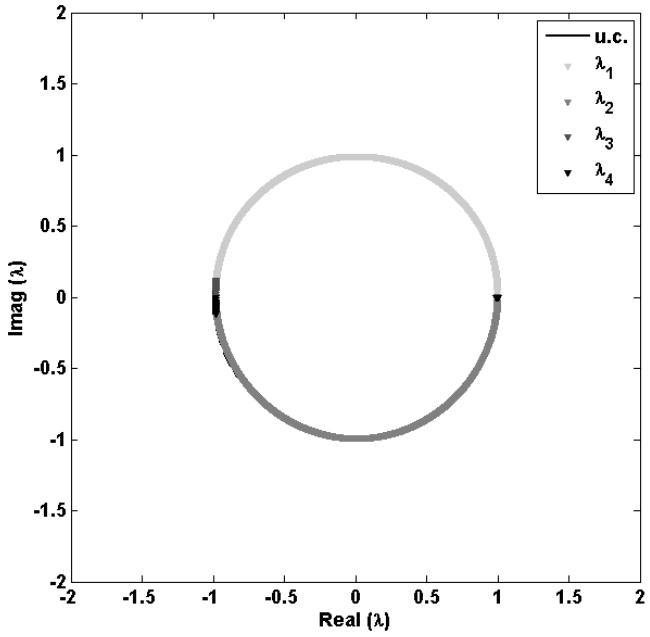

Figure 11: Distribution of the four roots in the complex coordinate plane with respect to combinations of wavenumber (k_x, k_z). The model considered is viscous fluid with $\Delta x = 2\times10^{-6}$ m, $\eta_\mu = 0.01$ kg/ms, and a relative smaller $\Delta t = 1.338\times10^{-9}$ s.

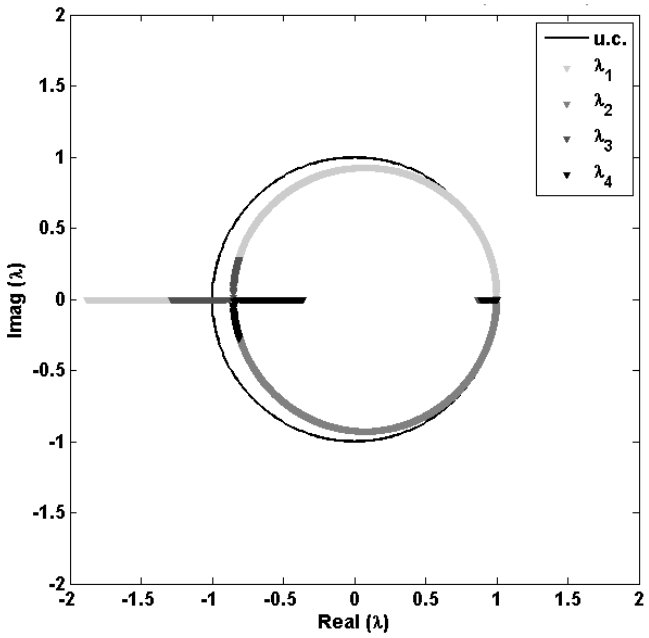

Figure 12: Distribution of the four roots in the complex coordinate plane with respect to combinations of wavenumber (k_x, k_z). The model considered is viscous fluid with $\Delta x = 2\times10^{-6}$ m, $\Delta t = 1.338\times10^{-9}$ s, and a greater viscosity $\eta_\mu = 0.1$ kg/ms.

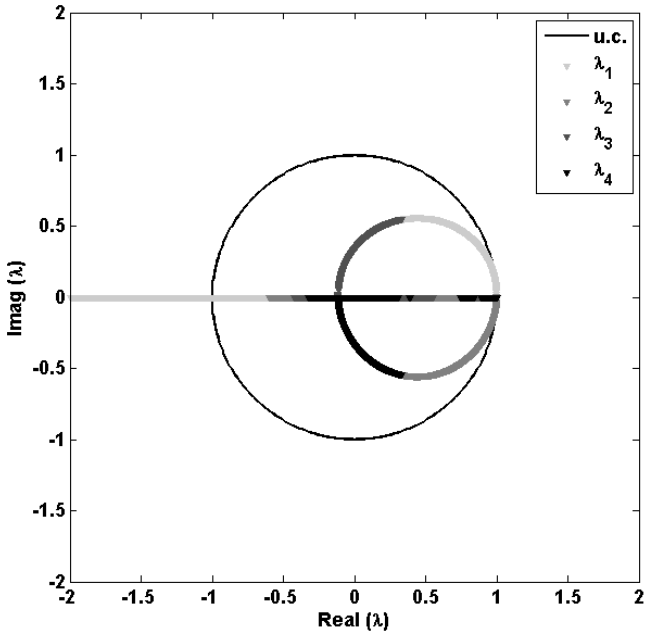

Figure 13: Distribution of the four roots in the complex coordinate plane with respect to combinations of wavenumber (k_x, k_z). The model considered is viscous fluid with $\Delta x = 2\times10^{-6}$ m, $\Delta t = 1.338\times10^{-9}$ s, and a much greater viscosity $\eta_\mu = 1$ kg/m s.

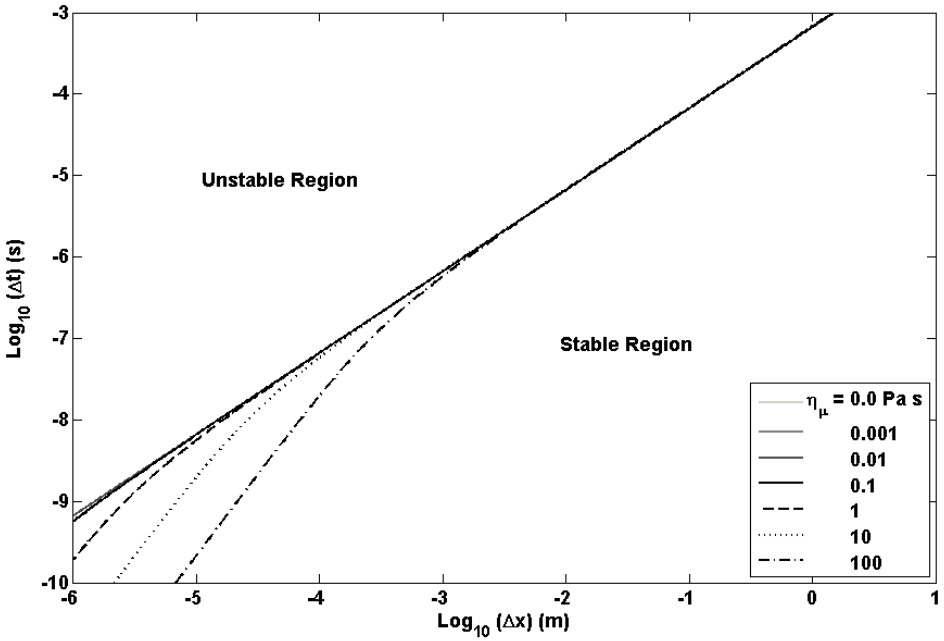

Figure 14: Distribution of the stable and unstable regions for the linearized Navier-Stokes equations after the von Neumann analysis.